Journal of
Applied Physics

ARTICLE

pubs.aip.org/aip/jap

Hybrid fluid particle-in-cell simulations of extreme-ultraviolet induced discharge

Cite as: J. Appl. Phys. **139**, 073301 (2026); doi: 10.1063/5.0309779
Submitted: 29 October 2025 · Accepted: 1 February 2026 ·
Published Online: 19 February 2026

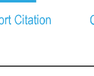

View Online Export Citation CrossMark

E. H. Kemaneci,[1,a)] D. Astakhov,[2] J. van Veldhoven,[3] A. Stodolna,[3] A. J. Storm,[3] L. C. J. Heijmans,[1] A. M. Yakunin,[1] and M. van de Kerkhof[1,4]

AFFILIATIONS

[1]ASML Netherlands B.V., Veldhoven, The Netherlands
[2]ISTEQ B. V., Eindhoven, The Netherlands
[3]TNO, Delft, The Netherlands
[4]Department of Applied Physics, Eindhoven University of Technology, Eindhoven, The Netherlands

[a)]**Author to whom correspondence should be addressed:** efe.kemaneci@asml.com

ABSTRACT

Hydrogen plasma interaction with materials in Extreme Ultraviolet (EUV) lithography systems plays a crucial role in determining component longevity and particle behavior. To evaluate material resilience and cleanliness under plasma exposure, experiments are conducted in the EUV Beam Line 2 (EBL2) infrastructure at TNO (Nederlandse Organisatie voor Toegepast Natuurwetenschappelijk Onderzoek). A comprehensive characterization of the EBL2 plasma environment is essential for understanding its impact on the analyzed sample. This study employs a three-dimensional hybrid Particle-in-Cell Monte Carlo (PIC/MC) simulation framework to investigate the spatiotemporal plasma conditions. A notable influence of a negative voltage leakage in the Retarding Field Energy Analyzer (RFEA) sensor is observed on ion flux and energy, that also enhances the agreement between simulations and measurements. The simulations further reveal transient in-beam ion energy flux distribution functions and electron energy distributions in the beam-focus, both of which still remain beyond current diagnostic capabilities.

22 April 2026 10:55:52

© *2026 Author(s). All article content, except where otherwise noted, is licensed under a Creative Commons Attribution (CC BY) license (https://creativecommons.org/licenses/by/4.0/).* https://doi.org/10.1063/5.0309779

I. INTRODUCTION

Extreme Ultraviolet (EUV) lithography has emerged as a pivotal technology in the semiconductor manufacturing industry, enabling the fabrication of advanced microelectronic devices with feature sizes as small as a few nanometers.[1,2] The interaction of high-energy photons with background gas leads to the formation of an EUV-induced plasma[3] that effectively sputters carbonaceous layers on the multilayer mirrors caused by the hydrocarbon contamination.[4,5] Material durability under exposure to such reactive species is imperative and a series of preliminary experiments are conducted in off-line discharges, e.g., electron-cyclotron-resonance,[6,7] electron-beam,[8] and EUV-induced (energy coupling) excitation mechanisms.[9]

The Extreme Ultraviolet Beam Line 2 (EBL2) facility at TNO[10] is an experimental platform designed for the characterization of EUV-induced plasmas and the accelerated testing of nanolithographic components. The facility integrates a Sn-based EUV source with a high-repetition-rate pulsed beam and a flexible exposure chamber capable of operating across a wide range of hydrogen pressures (5–20 Pa). The system enables detailed studies of plasma–surface interactions, critical for understanding component degradation and contamination in next-generation lithography. Understanding the underlying physical phenomena of the highly transient EUV-induced EBL2 plasma is crucial for proper exposure and diagnostics capabilities.

Prior work on EBL2 has characterized ion fluxes, energy distributions[11] by the use of a Retarding Field Energy Analyzer (RFEA). However, most of the underlying plasma mechanisms are still unresolved. The RFEA data exhibit delayed secondary flux at positions more than 14 mm away from the beam axis, the origin of which has yet to be identified. The spatiotemporally varying plasma dynamics produce sample-position-dependent particle and energy fluxes to the exposed surface, whereas in-beam RFEA

© Author(s) 2026

diagnostics are not feasible. Surface reactivity is further modulated by the mass of the incident ion composition; for instance, hydrogen, deuterium, and tritium ions exhibit distinct chemical sputtering yields when interacting with hydrocarbon surfaces.[12] In addition, low EUV-induced plasma afterglow potentials complicate diagnostics uncertainty. In particular, the sensitivity of RFEA measurements to sensor-grounding deviations remains unquantified, leaving the associated uncertainties unknown. These gaps motivate a complementary three-dimensional computational modeling approach to probe the mechanisms in detail and to interpret RFEA observables under EBL2 conditions.

The inherently transient and non-uniform characteristics of EUV-induced plasma, combined with weakly collisional and non-local behavior calls for kinetic simulation methods like Particle-In-Cell with Monte Carlo collisions (PIC/MC). This method has been extensively applied to explore various energy coupling mechanisms, e.g., capacitive,[13–16] microwave electron cyclotron resonance[17] and electron-beam generated plasmas,[18] while foundational insights are available in several key references.[19–24] Early applications to EUV-induced plasmas were conducted in one[25] and two dimensions.[26] Recent advancements have led to a three-dimensional hybrid PIC/MC model in order to capture the rapid EUV excitation and prolonged afterglow that aligns well with experimental ion flux and composition data.[27] A latest investigation employs an alternative hybrid methodology,[28] applied at relatively elevated powers and repetition rates.

Current investigation covers a three-dimensional hybrid PIC/MC model of the EBL2 exposure chamber. The details of the experimental setup are summarized in Sec. II, followed by modeling principles in Sec. III. Section IV focuses on the simulation results of spatiotemporal plasma behavior, ion flux composition, and evolution, a sensitivity analysis on a negative RFEA sensor voltage leakage (~ -1 V) as well as of in-beam ion and electron kinetics.

II. EXPERIMENTAL SETUP

The EBL2 system configuration and diagnostic framework are thoroughly documented by van Veldhoven *et al.*[11] and only a brief summary is provided here. The system components include a high-brightness source of EUV radiation, the collector module, and the exposure chamber, depicted in Fig. 1. The EUV source operates as a repetitively pulsed high-voltage discharge in vacuum, ignited between rotating disk electrodes covered by a thin liquid tin layer. The tin plasma produced in the discharge is rapidly heated by the current with a rise time of 100 ns. This results in a high-brightness burst of EUV radiation that propagates through the collector chamber, containing two grazing incidence mirrors, into the exposure chamber via the entrance cone. The incoming beam exhibits an annular intensity profile, as illustrated in the three-dimensional computational domain in Fig. 1. A convergent beam is formed in the exposure chamber, focusing to a diameter of about 1 mm. Once it passes the focus, the beam expands and subsequently reaches the sample surface with the annular defocused beam pattern;[11] its position within the computational domain is indicated accordingly. The repetitive light pulses vary in a range of 1.5–3 kHz, with an average duration of 80 ns per pulse. The source is optimized for operation at 3 kHz in this work, resulting in a radiant intensity of 80 W/(2πsr) measured at a wavelength of 13.5 nm ± 1%. The typical beam power varies between 2 and 5 W. The range is far below the hundreds-of-watts operating powers of typical lithography sources,[27,31] however the power density remains scalable with area.

The gas environments of the exposure chamber and the collector chamber are separated with an orifice by using differential pumping. The computational domain focuses particularly to a simplified form of the exposure chamber. It is schematically illustrated in Fig. 1 with the indicated incoming and de-focused radiation pattern. The focal point of the convergent beam is situated approximately 20 mm away from the surface. The location of the RFEA is depicted at 23 mm away from the beam center, which is mounted on the surface of the sample holder facing the EUV beam and radially moved to various locations. A background gas of hydrogen at a pressure of 5 Pa is considered in this study. A gas temperature of 300 (K) is assumed, with EUV-induced heating considered negligible since the plasma predominantly resides in a decaying state with a low photo-absorption coefficient. Analytical evaluation using the heat transport equation similarly supports this assumption, consistent with previous estimates.[32,33] In addition, a gas heating is not reported at higher repetition rates and power in a recent multiple-pulse computational investigation.[28] The temporal beam intensity profile, reported earlier,[29,30] is illustrated in Fig. 1. A measured wavelength spectrum is provided in a separate study[34] and the normalized count is shown in Fig. 2.

The RFEA is not operable directly in the beam, restricting experimental diagnostics to a minimum radial distance of 8 mm away. However, the simulations incorporate a hypothetical RFEA to estimate in-beam characteristics. Therefore, the computational domain assumes RFEA sensors situated at 0, 8, 16, and 23 mm from the beam's central line. The grounded surface of the RFEA is susceptible to negative voltage leakage due to its mesh-like structures and the negatively biased region beneath it. The simulations are carried out for either a grounded RFEA sensor with a diameter of about 1 cm or a fixed voltage at -1 V to capture the influence of a surface potential leakage.

III. MODEL

A three-dimensional electrostatic PIC/MC framework is formulated based on the kinetic equations governing plasma species, coupled self-consistently with the Poisson equation for electrostatic fields.[20] The framework employs an explicit, energy-conserving scheme.[35] A key advantage of this approach is that only the plasma frequency must be accurately resolved, allowing the computational cell size to exceed the Debye length.[22] This makes electron cooling through collisions with H_2 feasible and avoids an excessively fine three-dimensional mesh.

A brief overview of the model is presented, and further details are reported in prior work.[26,36,37] Mathematical representation for a plasma super-particle a of species i is expressed as follows:

$$\ddot{\vec{x}}_i^a = -\frac{q_a}{m_a}\nabla\phi, \tag{1}$$

$$\nabla^2\phi = \frac{\rho}{\varepsilon_0}, \tag{2}$$

22 April 2026 10:55:52

© Author(s) 2026

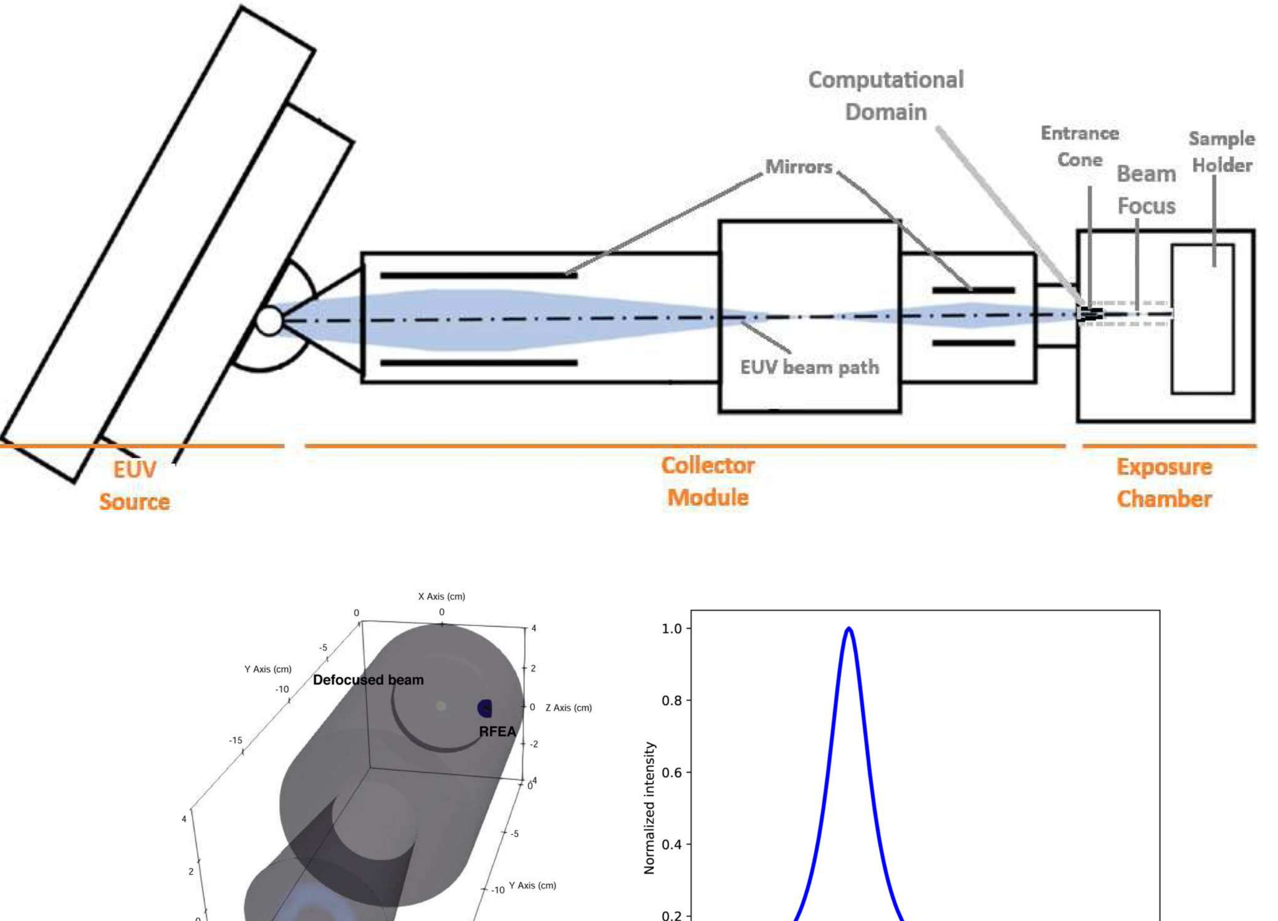

FIG. 1. (Top) A two-dimensional depiction of the EUV source, collector module, and exposure chamber together with beam path, grazing incidence mirrors as well as the computational domain. (Bottom-left) A three-dimensional representation of the computational domain for the EBL2 exposure chamber in a defocused beam configuration. The EUV pattern of the incoming beam and defocused beam are shown. The RFEA sensor, rendered in black, moves either toward the beam center or away from it. The considered locations of the RFEA in this study are 0, 8, 16, and 23 mm away from the beam center. (Bottom-right) Time-resolution of the normalized light intensity.[29,30] The intensity values less than or equal to that observed at $t = 0$ are assigned to zero.

22 April 2026 10:55:52

where m_a is the mass, q_a is the charge, ϕ is the electrostatic potential, and ρ is the plasma charge density. The computational domain is discretized by an unstructured tetrahedral mesh, a choice motivated by the robustness of available meshing tools for intricate geometries. In order to ensure accurate resolution of plasma phenomena in the computational domain, a finer computational mesh is employed within the EUV-irradiated region. Additionally, the grid is further refined in the vicinity of the sample holder to capture the space-charge potential and to match the resolution requirements of the RFEA sensor. The Poisson equation is solved using the finite element method with linear base elements. In combination with the energy-conserving formulation, this choice produces a piecewise-constant electric field within each element, since the spatial gradients of the linear basis functions are constant.

In order to mitigate the numerical noise introduced by a cell-wise constant electric field, we employ an event-detection-based time-domain substepping scheme. At each global time step, the algorithm checks whether a particle crosses any cell boundaries. If no crossing is detected, the particle is advanced with the standard velocity-Verlet integrator. If a crossing occurs, the step is

© Author(s) 2026

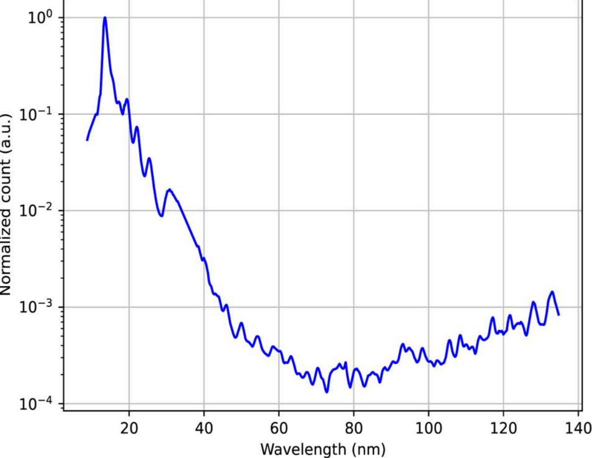

FIG. 2. Normalized EUV-source spectrum measured at EBL2, detailed elsewhere.[34]

partitioned into segments proportional to the particle's residence time in each cell. These fractional durations are recorded per particle and used in the velocity update of the Verlet scheme, ensuring a smooth transition between fast particles that traverse many cells in a single step and slow particles that remain within one cell over multiple steps.

Collisions between particles and with the background gas are sampled on each time step by the help of Nanbu scheme.[38] The set of cross sections used to compute collision probabilities includes interactions of electrons and ions with H_2. It should be emphasized that given the low degree of dissociation (estimated to be $<10^{-4}$) collisions of electrons and ions with atomic hydrogen (H) are neglected in this study.

The cross section set for electron collisions with H_2 is structured similarly to Ref. 39. It includes differential cross section data for excitations from Ref. 40 and for ionization from Ref. 41. Part of the cross section set for H^+ and H_3^+ interactions with H_2 is based on Refs. 43 and 42. Comprehensive details of the reaction set are available in Ref. 37 (pp. 39–44). The cross section set and the angle-dependent sampling routines are validated against experimental Swarm data. Good agreement is obtained for the electron drift velocity and the ionization coefficient, as well as for the mobility and diffusion of H^+ and H_3^+ in H_2. The data set is employed to model EUV-induced plasma and validated against measurements.[26,36] The exact data set is further utilized in a separate two-dimensional electromagnetic PIC/MC model of electron cyclotron discharges, with benchmarking performed using a range of probe diagnostics.[17] A key ion conversion reaction in the current study is

$$H_2^+ + H_2 \rightarrow H_3^+ + H. \tag{3}$$

Electron–ion pairs generated by photo-absorption of the EUV radiation are introduced into the simulation domain. The number of such pairs is defined according to a probability distribution, weighted by the spatiotemporal and spectral characteristics of the EUV pulse. The following photo-ionization processes are included:

$$H_2 + h\nu \rightarrow \begin{cases} H_2^+ + e, \\ H^+ + H + e. \end{cases} \tag{4}$$

Corresponding energy-dependent cross section data are adopted from a study by Chung *et al.*[44] with the resulting H_2^+ to H^+ ratio being approximately 5 at a wavelength of 13.5 nm. The energy assigned to each injected electron equals the photon energy—sampled from the EUV spectrum—minus the ionization potential of molecular hydrogen. Electrons are emitted with an angular distribution function described by unpolarized light.[36,45] In the current simulations, photo-ionization of atomic hydrogen is disregarded due to its minimal influence in order to enhance computational performance.

Irradiation of the chamber walls by EUV leads to photoelectron emission, which we model as a surface source of electrons. The spatiotemporal distribution of this source is prescribed by the EUV pulse. The emission yield is taken as ≈0.01 electrons per incident photon, representative of carbon-contaminated steel surfaces.[46] The energy distribution of the emitted electrons is sampled according to[47]

$$P(E) \sim E(E+W)^4, \tag{5}$$

where E is the emitted electron energy, $P(E)$ the emission probability, and W representing the work function of wall materials.

During the afterglow after EUV is switched off, the mean electron energy falls below 0.5 eV within a few μs, leaving no electrons above the minimum threshold of electronic excitation (~ 8 eV). Nevertheless, the plasma density remains sufficient to enforce a small explicit PIC time step (e.g., $\Delta t < 10^{-11}$ s). Under these conditions, we switch to a Hybrid-PIC mode to accelerate the computation: ions are retained as particles, whereas electrons are treated as a fluid. The electron initial density and energy are taken from the preceding PIC solution. The electron fluid model is described by the following set of equations under drift-diffusion approximation:

$$\frac{\partial n_e}{\partial t} + \nabla\left(-\mu_e n_e \vec{E} - D_e \nabla n_e\right) = 0, \tag{6}$$

$$\frac{\partial\left(n_e \frac{3}{2} k_B T_e\right)}{\partial t} + \nabla\left(-\frac{5}{2}\frac{k_B^2}{q_e} T_e \mu_e n_e \nabla T_e - \frac{5}{2} k_B T_e \frac{j_e}{q_e}\right) = \vec{E} j_e + S_{eE}, \tag{7}$$

where n_e is the electron density, μ_e the electron mobility, D_e electron diffusion coefficient, $\vec{E}$ electric field, T_e electron temperature, j_e current density, and S_{eE} is the volumetric sink of electron energy due to collisions with H_2. The coupling between the electron fluid and ion kinetic models is achieved through the plasma charge density in the Poisson equation and finite volume approximation is used in the numerical solution of the electron fluid equations.

The modular workflow and data exchange process for the PIC and Hybrid-PIC approaches are depicted in Fig. 3, following the standard PIC cycle widely recognized in the literature. A switch

22 April 2026 10:55:52

© Author(s) 2026

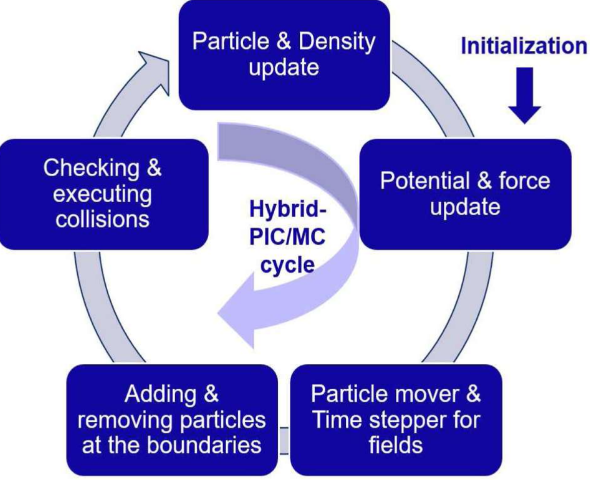

FIG. 3. PIC and Hybrid-PIC cycle.

condition from PIC to Hybrid-PIC modes is set as electron energy distribution function (EEDF) that exhibits Maxwellian behavior with mean energy below 0.5 eV, long after the EUV is switched off.[27] In the EBL2 specifications, this corresponds to 3 μs, where both PIC and Hybrid-PIC are computed between 3 and 5 μs. Only Hybrid-PIC is simulated until the next EUV pulse [e.g., 333.33 (μs)]. The simulations are performed until a periodic-steady-state is established, corresponding to a few consecutive EUV pulses with the aforementioned switching scheme between PIC and Hybrid-PIC. As a caveat, reaching this state demands two pulses at the specified EBL2 operation parameters, which is far fewer than under scenarios involving greater repetition rates and power levels.[28,48]

IV. RESULTS

The simulations are earlier benchmarked against experimental diagnostics of EUV-generated hydrogen plasmas to ensure the accuracy, such as electron density profiles,[36] probe response signals,[26] and ion flux and composition ratios.[27] This section focuses on the general plasma behavior and compares it with measured ion fluxes. Subsequently, the impact of RFEA sensor voltage leakage is computationally examined by either grounding the sensor or setting it to -1 V. The in-beam ion kinetics are then discussed, followed by a time-resolved analysis of electron dynamics.

Figure 4 illustrates the time evolution of the electron density and potential contours on the $x = 0$ plane from the beam center. At 1 ns into the simulation, remnants of electrons from the prior EUV pulse are still present. Photo-induced secondary electron emission with energy sampled by Eq. (5) produces a dense electron cloud near the surface, where the beam impinges upon and the potential drops down to -10 V. The spatial inhomogeneity is visible toward the end of the computational domain. The imprint of the EUV beam's annular-shaped distribution becomes visible in the electron density and potential maps at 61 ns, located between the beam focus and incident surface. The beam focus leads to steep potential peaks, reaching up to locally 100 V at the beam focus, 50 V in the incident beam region, and 20 V in the de-focused area. The earlier secondary electron cloud is pushed to the side of the de-focused beam. At 111 ns, the EUV beam intensity has weakened significantly, making the transition of the plasma into its decay phase. Central electrons continue to contribute to ionization, increasing ion density, while the previously observed high potential values subside. The internal potential drops to around 30 V, and the surrounding negative potential cloud dissipates. The annular-shaped structure is still visible in the spatial distribution. The EUV beam is turned off and the plasma enters its decay phase of a long afterglow at 151 ns. As the ionization continues, the plasma potential gradually declines. The electron density peaks in a central cylindrical region, loosing the earlier toroidal-shape print. Electron densities, which momentarily reached to 1×10^{12} (cm^{-3}) inside the beam, start to decrease. At 211 and 501 ns, energetic electrons still persist and newly formed ions reduces the potential. The central electron density gradually settles down to the values seen at 1 ns 1×10^{9} (cm^{-3}).

Net ion fluxes measured by the RFEA at positions (a) 8, (b) 16, and (c) 23 mm are compared with results from PIC and Hybrid-PIC simulations in Fig. 5. The exact values of the diagnostics errors are absent but a generic 30% is assumed in parallel with the earlier publication.[11] The experimental and calculated fluxes are in close agreement at each RFEA location. The model anticipates the measured secondary peak at 1.5 μs on 16 mm and at 2.0 μs on 23 mm. On the other hand, the simulations predict a comparatively faster temporal decay rate. The observed difference of the decay rate may be attributed to the enhanced photo-ionization from plasma photons or a transient VUV/DUV tail of the EUV source. A higher noise amplitude is observed in the simulations at positions farther from the beam axis due to the declining ion density profile. The onset of the hybrid simulations is set at 3 μs. Comparison of the PIC and Hybrid-PIC in the ion flux between 3 and 5 μs shows a close match, indicating the validity of fluid electron treatment.

Figure 6 illustrates the simulated ion flux composition together with the net measured values at (a) 8, (b) 16, and (c) 23 mm. A shift of the dominant ion type causes the secondary flux peaks observed at 16 and 23 mm. The main photo-ionization via process (4) and electron-impact-ionization product is H_2^+, with H^+ forming at a lower branching ratio. Closer to the beam H_2^+ prevails whereas, the atomic ion is the main flux contributor at 16 and 23 mm due to relatively smaller loss rate. The photo-ionization products peak below 1 μs and they subsequently form H_3^+ ion by reaction (3) as a dominant positive charge till the next EUV pulse.

A. Influence of a negative RFEA voltage leakage

The comparison of measured and simulated peak ion energies is shown in Fig. 7 at radial positions of 8, 16, and 23 mm. The simulations are carried out at either a grounded RFEA sensor or one held at -1 V, corresponding approximately to the diagnostic energy-measurement uncertainty. The ion composition follows the proportions indicated in Fig. 6. The simulations indicate that ions

22 April 2026 10:55:52

© Author(s) 2026

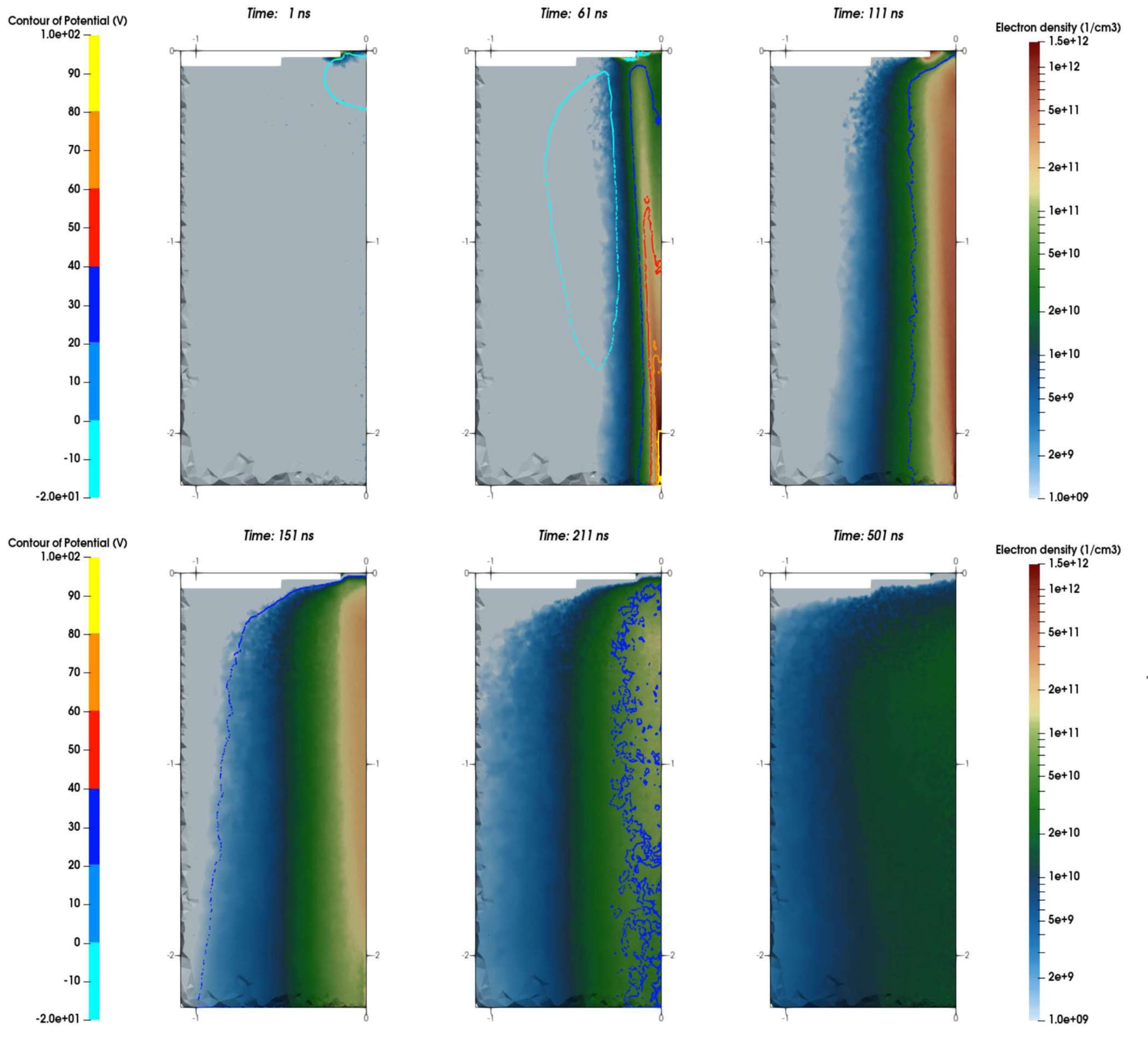

FIG. 4. Temporal evolution of the electron density and electrostatic potential contours within the first 500 ns on the clipped central axial plane ($x = 0$) from the radial beam symmetry axis. Triangular structures on the edges are due to three-dimensional clipping.

may attain peak energies as high as 70 eV in-average during EUV exposure independent of the radial distance. As a caveat, individual signals of 100 eV ions are spotted at the 16 and 23 mm RFEA positions as well as 80 eV at 8 mm. These features are due to local temporal potential variation illustrated in Fig. 4 and they disappear in the smoothened data. The time at which the maximum peak energy occurs is delayed, moving further from the beam. Influence of the sensor voltage is negligible on the simulations up to 2 μs, afterwards negatively biased sensor energies settle toward the leakage level while the grounded sensor energy continues decaying. Measurements converges to 2 eV within 2–5 μs, and a voltage leakage of −1 V better estimates this observation.

Figure 8 presents a comparison between the measured and simulated ion flux energy distribution functions (IFEDFs) on an 8 mm RFEA at (a) 1 μs, (b) 2 μs, and (c) 3 μs. An assumption of 30% diagnostics error bar are depicted that increases with an

22 April 2026 10:55:52

© Author(s) 2026

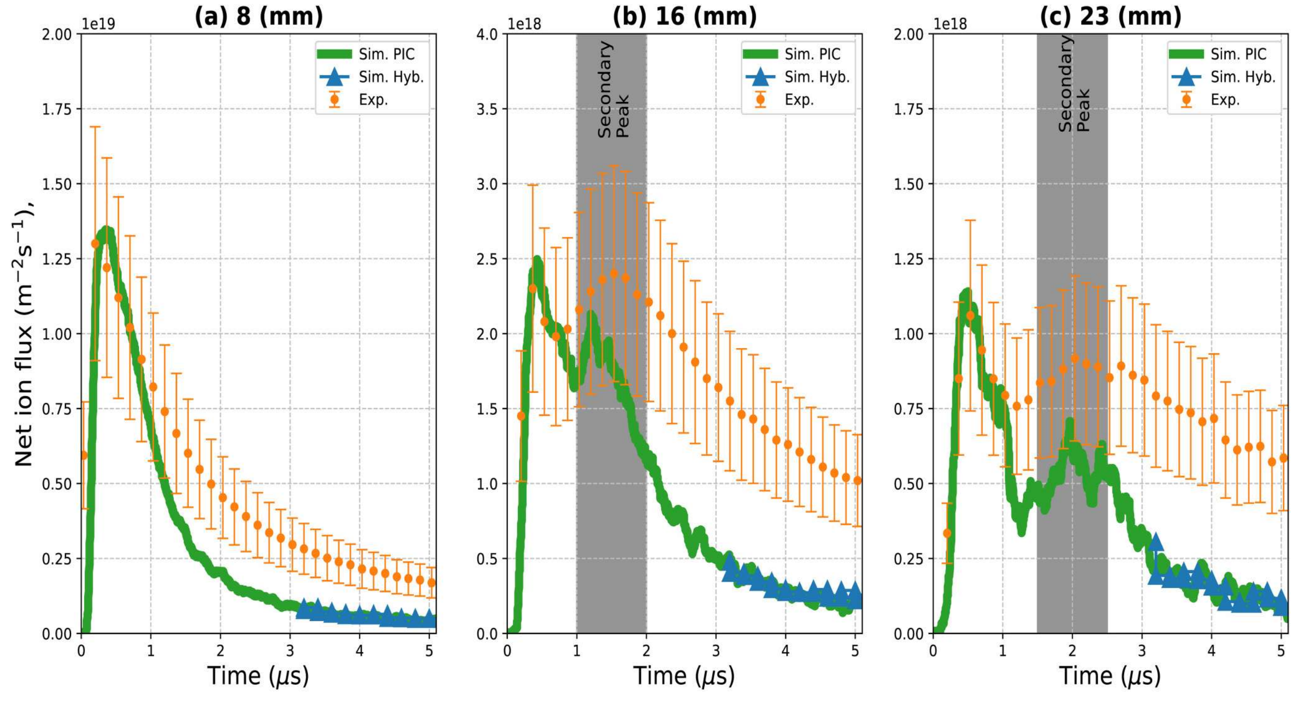

FIG. 5. Comparison of simulated (PIC/MC and Hybrid-PIC/MC) and experimentally measured net ion fluxes on the RFEA at positions (a) 8 mm, (b) 16 mm, and (c) 23 mm. Measurement uncertainties are estimated at 30%, and hybrid simulations are initialized at 3 μs. A grounded RFEA sensor configuration is used in the simulations.

22 April 2026 10:55:52

increasing energy value. Both dat asets reveal a temporal shift of the peak toward zero, while simulations demonstrate a clear sensitivity on the sensor voltage in larger timescales. The influence of voltage variation on the calculated IFEDF becomes evident after 2 μs mark. The simulations with a voltage leakage show better agreement with measurements at 3 μs.

A comparison of the afterglow ion flux measurements and calculations by Hybrid-PIC at (a) 8 mm, (b) 16 mm, and (c) 23 mm

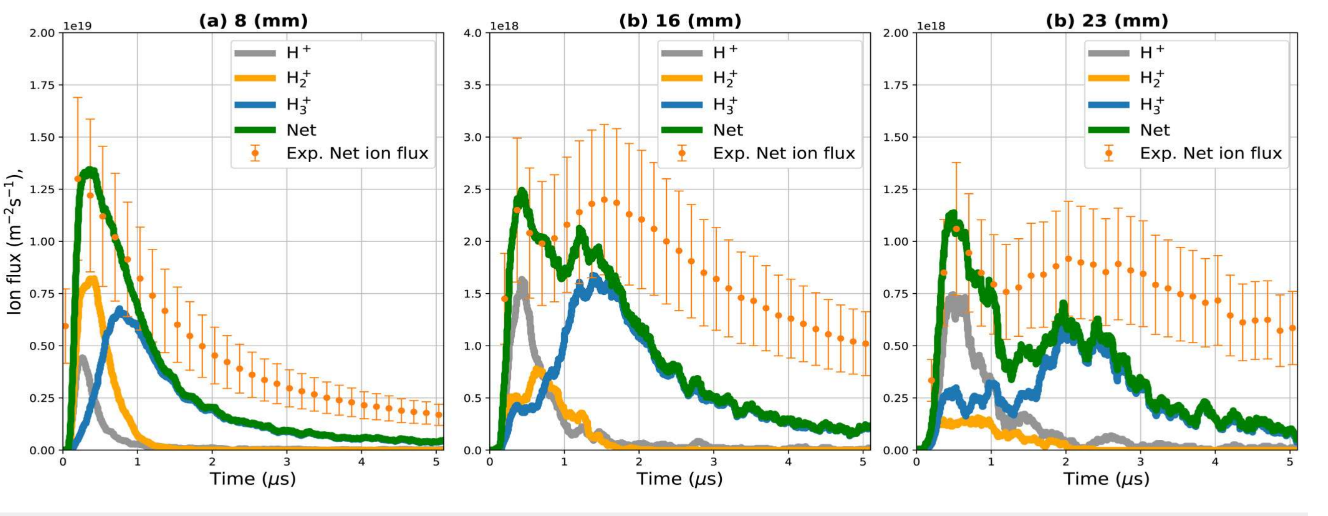

FIG. 6. Simulated (PIC) ion composition and measured net ion flux on the RFEA at (a) 8 mm, (b) 16 mm, and (c) 23 mm.

© Author(s) 2026

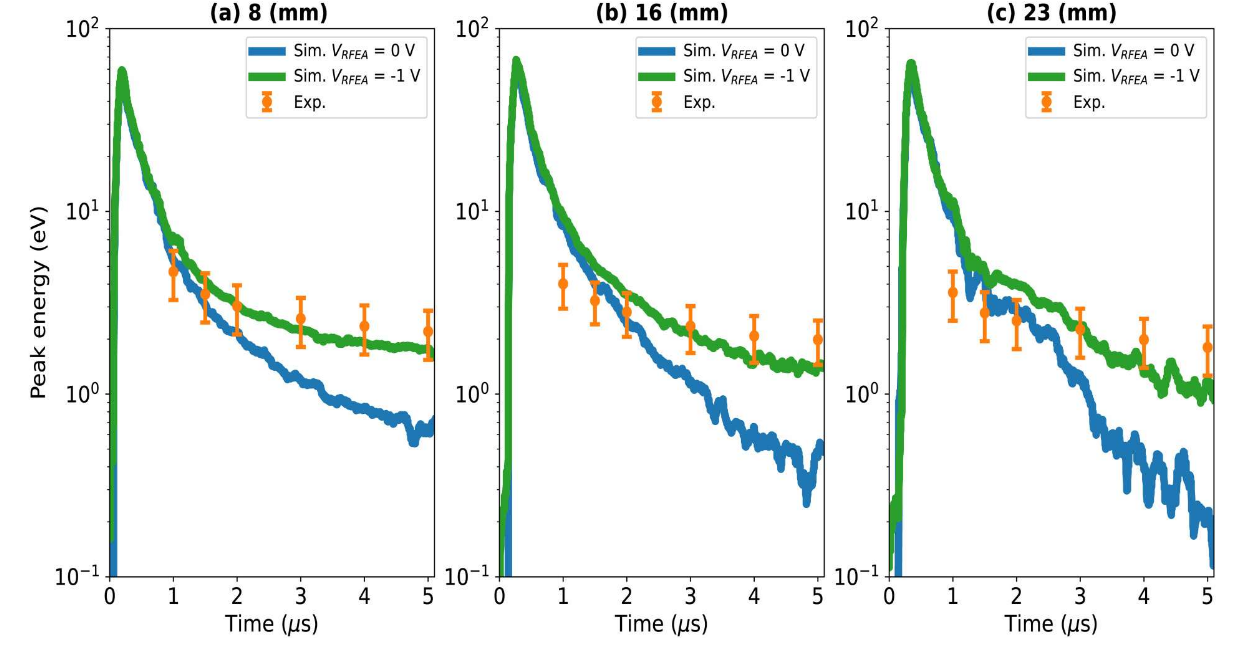

FIG. 7. Simulated (PIC) and measured peak ion energy on the RFEA at (a) 8, (b) 16 and (c) 23 millimeters. A 30% error is assumed in the measurements and PIC simulations are run at grounded and −1 V RFEA sensor.

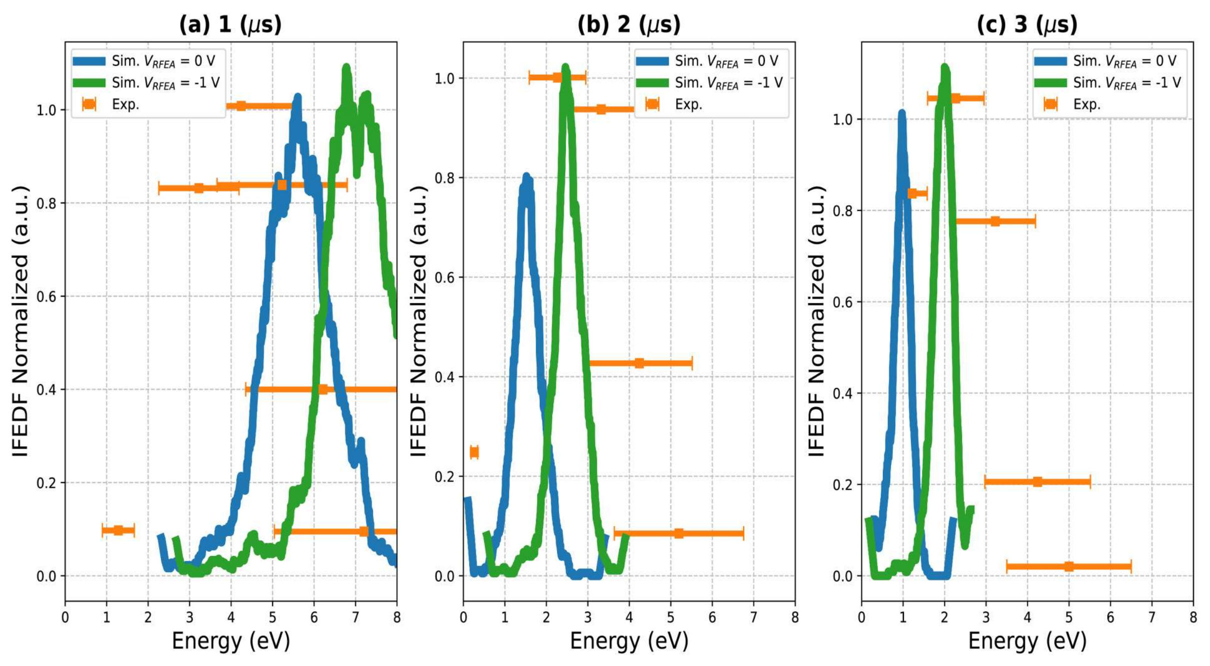

FIG. 8. Simulated (PIC) and measured IFEDF on the RFEA at 8 mm on (a) 1 μs ,(b) 2 μs, and (c) 3 μs. A 30% error is assumed in the measurements and PIC simulations are run at grounded and −1 V RFEA sensor.

22 April 2026 10:55:52

© Author(s) 2026

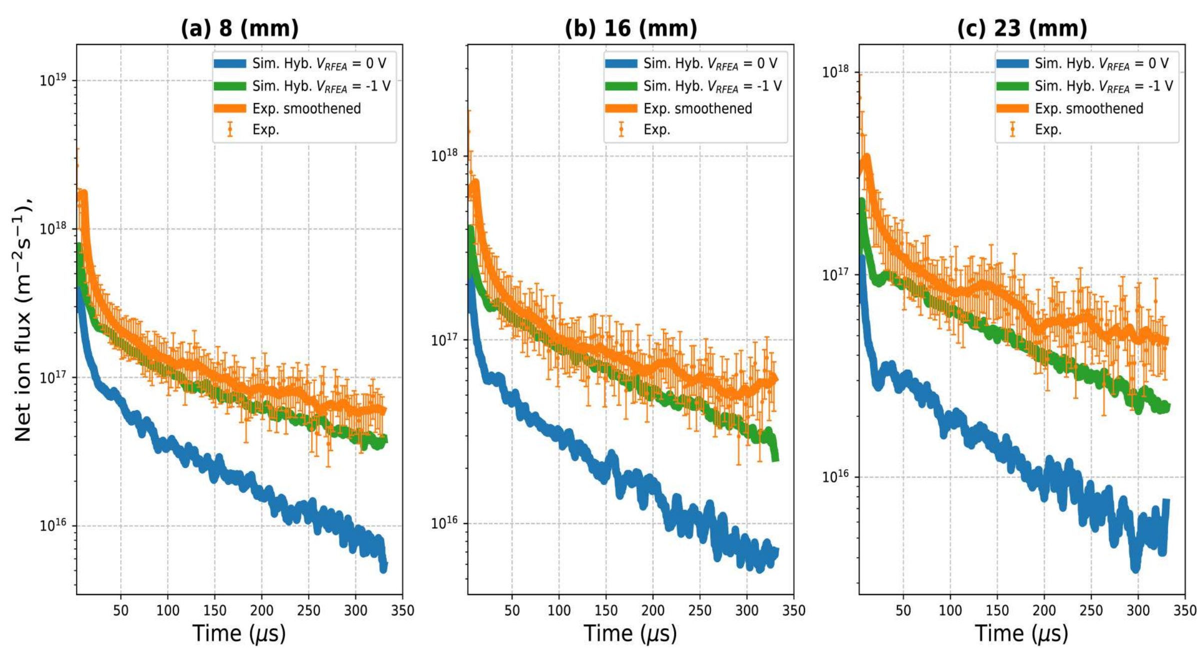

FIG. 9. Simulated (Hybrid-PIC/MC) and measured peak ion flux on the RFEA at (a) 8 mm (b) 16 mm and (c) 23 mm. A 30% error is assumed in the measurements and Hybrid-PIC simulations are run at grounded and −1 V RFEA sensor.

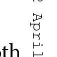
22 April 2026 10:55:52

RFEA locations are provided in Fig. 9. Due to negative potential leakage, the ion flux shows a slight increase in the early microseconds, which escalates to a tenfold enhancement by the end of the EUV pulse, regardless of the RFEA location with respect to the beam. The final ion flux levels become nearly identical at all measurement points, indicating that spatial homogeneity has been achieved within the domain. In addition, a voltage leakage of about −1 V significantly enhances the agreement between the experimental measurements and the simulation results during the afterglow period.

B. In-beam ion and electron kinetics

Figure 10 shows the species-resolved IFEDF evolution in first 500 ns on and in-beam RFEA sensor, together with snapshots of the voltage profile along the central beam line. Between 21 and 101 ns [Fig. 10(d)], potential settles to 40 V in the beam focus location, that locally and temporally reaches up to 100 V in the earlier phase of the pulse (see Fig. 4 for two-dimensional potential at 61 ns). This transient potential drop accelerates the energetic ions - averaged over the timescale of 50–100 ns [Fig. 10(a)], extending their energies up to 60 eV for the photo-ionization products of H_2^+ and H^+. It is worth noting that the peak ion energy decreases as the RFEA position approaches the beam axis, attaining its minimum in-beam location (not shown here). In addition, the time of the maximum peak ion energy shifts later by tens of nanoseconds with increasing distance from the beam center. We attribute this to the shorter ion acceleration times under electric fields within this time period before the quasineutrality established. Both distributions show similar trends with respect to the energy, however larger branching ratio of H_2^+ relative to that of H^+ is clearly visible on the absolute flux values. The contribution of H_3^+ remains minimal at this timescale as its formation occurs through charge exchange reaction between H_2^+ and background hydrogen molecules.

Following EUV termination, the potential plateaus around 23 V in Fig. 10(e) at 201 ns. IFEDFs averaged over 150–200 ns in Fig. 10(b) peak around 30 eV with the most dominant flux still belonging to H_2^+. The generation of H_3^+ leads similar flux scales to that of H^+. Between 450 and 500 ns in Fig. 10(c), the energetic ions mostly disappear and IFEDF peak about 12 eV, that scales with the potential value reaching up to 9 V at 501 ns. H_3^+ dominates the peak flux yet H^+ shows the dominant flux in between 7 and 8 eV. The molecular ion distributions exhibit a highly similar profile with each tail stretching up to 15 eV. A much longer energy tail is observed for the atomic ion H^+ with individual energetic signals seen up to 30 eV. This is in agreement with the earlier diagnostics in a different setup,[49,50] where H_3^+ ions dominate the ion flux and that H^+ ions exhibit an energetic tail. This is due to fact that energetic H^+ has smaller loss rates with the collisions compared to H_2^+ and H_3^+.

The IFEDFs during afterglow are shown in Fig. 11 at (a) 1 μs, (b) 2 μs, and (c) 3 μs for an either grounded or negatively biased in-beam RFEA sensors. The maximum energies observed are notably reduced relative to earlier stages (illustrated in Fig. 10). The profiles closely match those recorded by the RFEA sensor located 8 mm

© Author(s) 2026

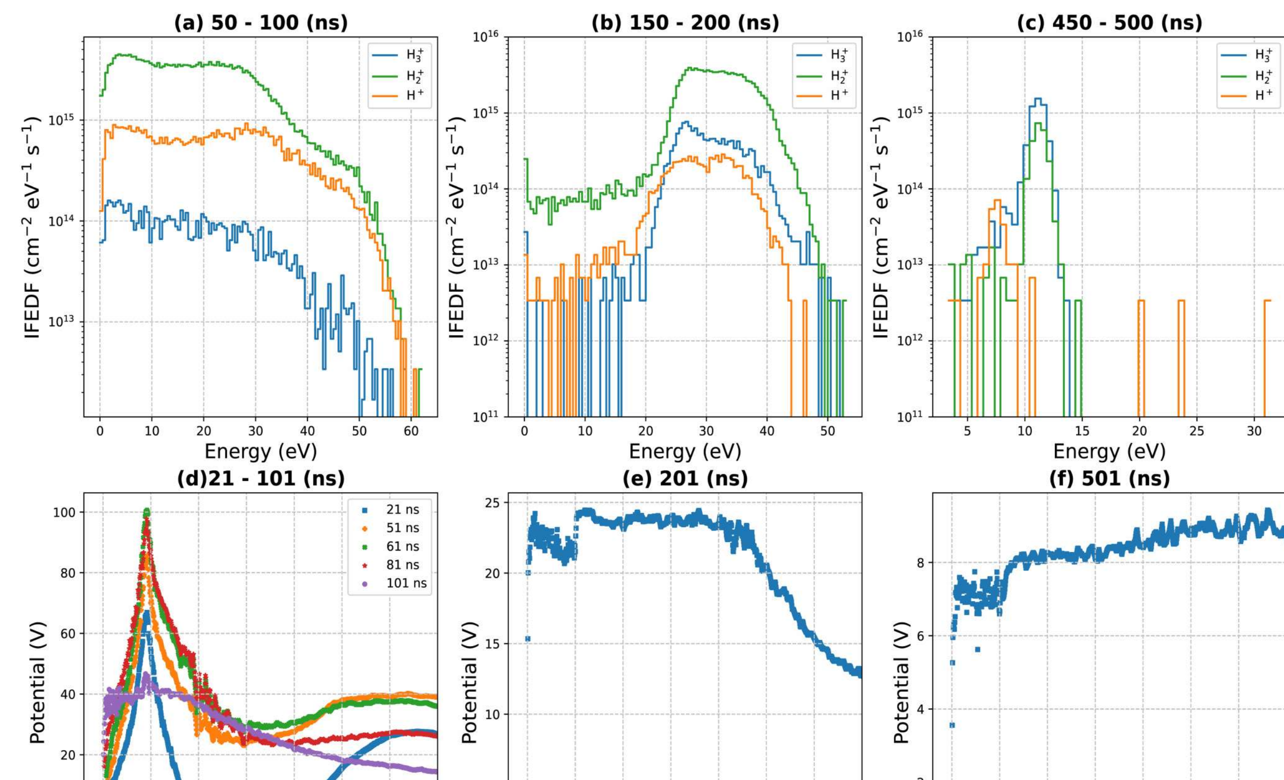

FIG. 10. Species-resolved time-evolution of IFEDF on an in-beam RFEA sensor (0 mm) averaged over the range of (a) 50–100 ns, (b) 150–200 ns, (c) 450–500 ns and snapshots of electric potential at the center of the beam at (d) 21 till 101 ns, (e) 201 ns, and (f) 501 ns. Distance of 0 cm represents the RFEA sensor surface.

22 April 2026 10:55:52

off-beam (shown 8), with a similar influence of a negative voltage leakage for the in-beam sensor. This reflects the spatial uniformity achieved in the beam's immediate vicinity during the afterglow.

The net ion flux profiles are compared across different RFEA positions in Fig. 12 relative to the beam center spanned up to 2000 ns. The peak ion flux increases as the RFEA sensor approaches the beam center, stretching up to a value of 3×10^{21} ($m^{-1}\,s^{-1}$). Increasing the distance between the RFEA sensor and the beam results in a reduced net ion flux and introduces a temporal delay of the order of tens of nanoseconds. Net ion flux recorded by the in-beam and 8 mm away sensors coalesce to identical values on 800 ns mark. The rest of the sensor locations are exposed to relatively smaller doses. The flux in all locations plateaus at about 3×10^{18} ($m^{-1}\,s^{-1}$) with an exception of the one at 23 mm away from the beam.

A weak ion signal appears on the sensors 8 and 16 mm away from the beam-center during active EUV exposure, presumably due to the ions escaping the beam region. This corresponds to the timescales before the development of a stationary plasma sheath structure. A secondary peak appears on the in-beam RFEA that is not visible on the rest of the sensor locations. This corresponds to EUV switch-off time and electron generation abruptly ceases. This instant decoupling of the power initiates a fast plasma expansion and further modifies the sheath properties. An establishment of a detailed physical mechanism demands a dedicated empirical investigation.

Simulated time-resolved electron energy distribution function (EEDF) at the beam focus is shown in Fig. 13. EUV photo-electron energy corresponds to 76 eV, calculated by subtracting the ionization threshold from the photon energy. At 200 ns, the energy is distributed efficiently across the entire energy spectrum, with a visible shoulder around 76 eV. The low energy region represents the secondary electrons created in the plasma volume. Energetic electrons continue to accelerate till 800 ns up to 175 eV due to the presence of high potential variation, where quasi-neutrality is not yet established. This aligns with the potential profile extending up to a localized peak of 100 V at the beam focus, as presented in Figs. 4

© Author(s) 2026

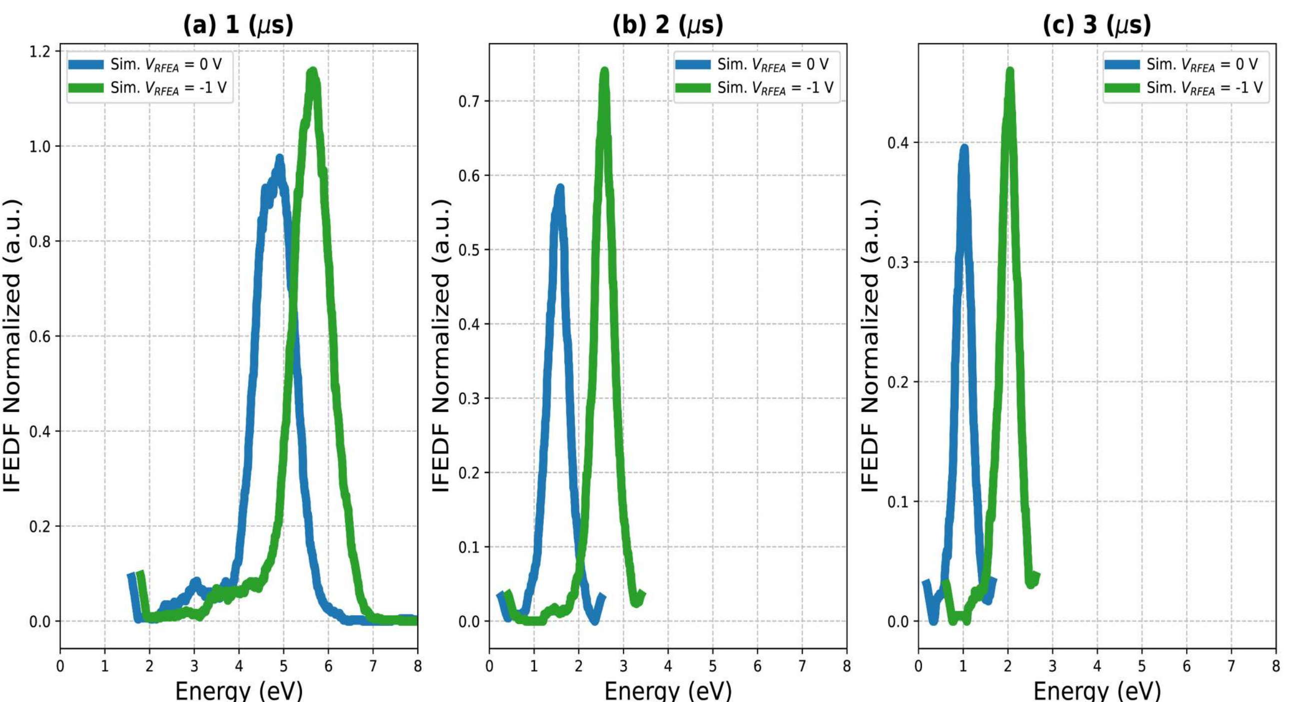

FIG. 11. Simulated (PIC) net ion energy flux distribution function on the RFEA at 0 mm on (a) 1 μs (b) 2 μs and (c) 3 μs. PIC simulations are run at grounded and −1 V RFEA sensor.

22 April 2026 10:55:52

and 10. The EEDF tail depletes gradually and fades significantly at 1000 ns with an effective Maxwellian electron temperature approximation of 0.5 eV. The EEDF tail falls beneath 30 eV around 1600 ns and by 3000 ns, the distribution settles into a Maxwellian form with a maximum energy below 25 eV and electron temperature of 0.2 eV. Hybrid-PIC simulations are initiated at the Maxwellization time of 3000 ns, where the electrons are treated by a fluid representation.

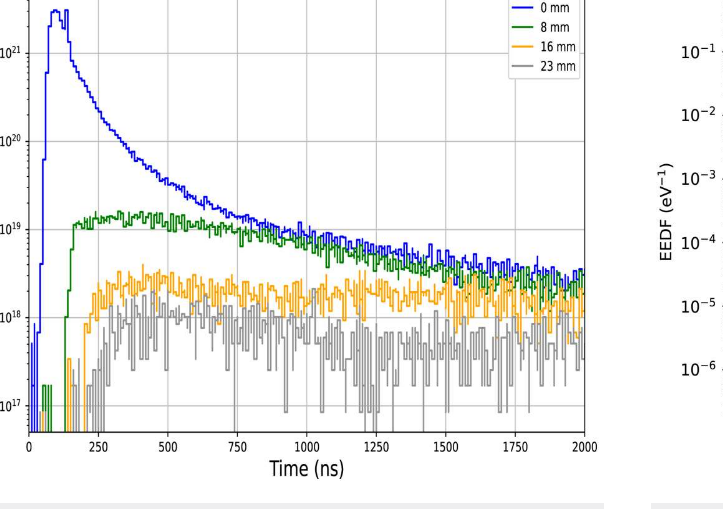

FIG. 12. Simulated net temporally-resolved ion flux till 2000 ns at different RFEA locations.

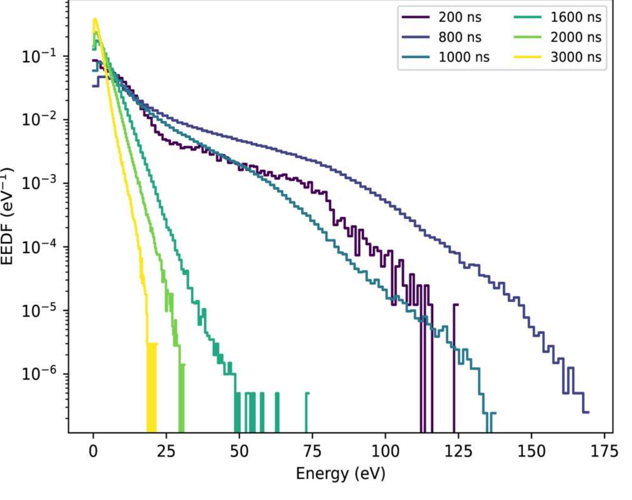

FIG. 13. Evolution of electron energy distribution function (1/eV) at the beam focus location.

© Author(s) 2026

V. CONCLUSIONS

A combination of PIC and Hybrid-PIC model is developed to characterize the EBL2 radiation generated plasma exposure tool along with the out-of-beam RFEA diagnostics. A strong transient plasma state is triggered by the brief EUV exposure, resulting in plasma voltage values up to 100 V locally. In the first few microseconds, the flux derived from measurements and simulations aligns closely, across varying sensor distances from the beam center. During this interval, the consistency between PIC and Hybrid-PIC results supports the validity of the chosen switch time for fluid electron treatment. The simulations reveal that the efficient conversion of H_2^+ and H^+ into H_3^+ is responsible for the secondary peak in far-flux values.

A negative voltage leakage of −1 V on the RFEA sensor is shown to play a critical role in influencing the recorded measurements. Initial flux data remain largely unaffected by the voltage leakage; however, its impact grows over time, resulting in higher flux readings on the sensor. The dominant impact of the leakage manifests in the ion energy flux distribution functions and peak energy during the plasma and subsequent afterglow periods. Simulation-measurement consistency during the afterglow phase is markedly improved when the leakage is considered. Super-elastic electron heating via vibrationally excited hydrogen molecules has been proposed as an alternative 2 eV ion afterglow sheath acceleration mechanism,[3] in parallel with the phenomenon in inductive discharge.[51,52] However, simulated vibrational population remains negligible owing to the much larger gap between afterglow period and power deposition duration of active EUV exposure. A further analysis of the phenomena is a prerequisite for a better understanding.

In-beam ion flux characteristics are not yet diagnostically accessible and the simulations conclude a strongly time-dependent in-beam IFEDF up to 500 ns. The acceleration scheme is driven by the highly dynamic voltage difference and cannot be accurately described by stationary sheath models in the initial hundreds of nanoseconds. Following the early transient dynamics, a decaying sheath description remains a suitable approximation. The longer tail of H^+ IFEDF compared to those of molecular ions[49,50] emerges only after 500 ns and is attributed to the low efficiency of atomic ion collisions. Compared to the out-of-beam calculations located 8 mm from the beam center, the in-beam peak flux is significantly higher, though both flux values and IFEDFs become similar after approximately 1 μs. The electron energy distribution function in the beam focus remains far from Maxwellian for the initial 3 μs.

ACKNOWLEDGMENTS

The work was conducted in the framework of ASML. The EBL2AV TKI project is funded by Holland High Tech–TKI HSTM via the PPS allowance scheme for public–private partnerships.

AUTHOR DECLARATIONS

Conflict of Interest

The authors have no conflicts to disclose.

Author Contributions

E. H. Kemaneci: Conceptualization (lead); Data curation (lead); Formal analysis (lead); Funding acquisition (lead); Investigation (lead); Methodology (lead); Project administration (lead); Resources (lead); Software (lead); Supervision (lead); Validation (lead); Visualization (lead); Writing – original draft (lead); Writing – review & editing (lead). **D. Astakhov:** Methodology (equal); Resources (equal); Software (equal). **J. van Veldhoven:** Data curation (equal). **A. Stodolna:** Data curation (equal). **A. J. Storm:** Data curation (equal); Formal analysis (equal); Investigation (equal); Writing – review & editing (equal). **L. C. J. Heijmans:** Writing – review & editing (equal). **A. M. Yakunin:** Funding acquisition (equal); Project administration (equal); Resources (equal); Writing – review & editing (equal). **M. van de Kerkhof:** Formal analysis (equal); Funding acquisition (equal); Resources (equal); Writing – review & editing (equal).

DATA AVAILABILITY

The data that support the findings of this study are available from the corresponding author upon reasonable request.

REFERENCES

[1]M. van de Kerkhof, H. Jasper, L. Levasier, R. Peeters, R. van Es, J.-W. Bosker, A. Zdravkov, E. Lenderink, F. Evangelista, P. Broman, B. Bilski, and T. Last, Proc. SPIE **10143**, 101430D (2017).
[2]R. van Es, M. van de Kerkhof, A. Minnaert, G. Fisser, J. de Klerk, J. Smits, R. Moors, E. Verhoeven, L. Levasier, R. Peeters, M. Pieters, and H. Meiling, Proc. SPIE **10583**, 105830H (2018).
[3]T. van de Ven, "Ion fluxes towards surfaces exposed to EUV-induced plasmas," Ph.D. thesis (Applied Physics and Science Education, 2018), Proefschrift.
[4]J. Hollenshead and L. Klebanoff, J. Vac. Sci. Technol. B **24**, 64 (2006).
[5]E. Kemaneci, A. von Keudell, L. Heijmans, A. M. Yakunin, and M. van de Kerkhof, J. Appl. Phys. **136**, 043301 (2024).
[6]D. Shefer, A. Nikipelov, M. van de Kerkhof, Z. Marvi, V. Banine, and J. Beckers, J. Phys. D: Appl. Phys. **56**, 085204 (2023).
[7]L. W. M. Bogaers, "Langmuir probe and spectroscopic measurements of electrons and H atoms in a low-pressure H_2 discharge," M.Sc. thesis, Eindhoven University of Technology, 2021. https://pure.tue.nl/ws/portalfiles/portal/247710969/0999926_Bogaers_L.W.M.J._MSc_thesis_MAP.pdf
[8]A. S. Stodolna, T. W. Mechielsen, P. van der Walle, C. Meekes, and H. Lensen, J. Vac. Sci. Technol. B **42**, 052601 (2024).
[9]E. te Sligte, N. Koster, F. Molkenboer, P. van der Walle, P. Muilwijk, W. Mulckhuyse, B. Oostdijck, C. Hollemans, B. Nijland, P. Kerkhof, M. van Putten, A. Hoogstrate, and A. Deutz, Proc. SPIE **9985**, 998520 (2016).
[10]H. Bekman, M. Dekker, R. Ebeling, J. Janssen, N. Koster, J. Meijlink, F. Molkenboer, K. Nicolai, M. van Putten, C. Rijnsent, A. Storm, J. Stortelder, C.-C. Wu, and R. de Zanger, Proc. SPIE **11147**, 1114706 (2019).
[11]J. van Veldhoven, C.-C. Wu, A. J. Storm, M. van Putten, J. R. Meijlink, and A. G. Ushakov, J. Vac. Sci. Technol. B **41**, 012603 (2023).
[12]W. Jacob, C. Hopf, M. Meier, and T. Schwarz-Selinger, in *Nuclear Fusion Research: Understanding Plasma-Surface Interactions*, Springer Series in Chemical Physics Vol. 78, edited by R. E. H. Clark and D. Reiter (Springer, Berlin, 2005), Chap. 11, pp. 250–285.
[13]Z. Donko, J. Schulze, B. G. Heil, and U. Czarnetzki, J. Phys. D: Appl. Phys. **42**, 025205 (2009).
[14]S. Wilczek, J. Schulze, R. P. Brinkmann, Z. Donko, J. Trieschmann, and T. Mussenbrock, J. Appl. Phys. **127**, 181101 (2020).
[15]J. T. Gudmundsson, J. Krek, D.-Q. Wen, E. Kawamura, and M. A. Lieberman, Plasma Sources Sci. Technol. **30**, 125011 (2021).

22 April 2026 10:55:52

© Author(s) 2026

[16]D. Eremin, E. Kemaneci, M. Matsukuma, T. Mussenbrock, and R. P. Brinkmann, Plasma Sources Sci. Technol. **32**, 044007 (2023).
[17]D. Eremin, Y. Sharova, L. Heijmans, A. M. Yakunin, M. van de Kerkhof, R. P. Brinkmann, and E. Kemaneci, Plasma Sources Sci. Technol. **34**, 065001 (2025).
[18]S. Rauf, D. Sydorenko, S. Jubin, W. Villafana, S. Ethier, A. Khrabrov, and I. Kaganovich, Plasma Sources Sci. Technol. **32**, 055009 (2023).
[19]M. A. Lieberman and A. J. Lichtenberg, *Principles of Plasma Discharges and Materials Processing* (John Wiley & Sons, NJ, 2005).
[20]C. K. Birdsall and A. B. Langdon, *Plasma Physics via Computer Simulation* (McGraw-Hill, New York, 1985).
[21]L. Brieda, *Plasma Simulations by Example* (McGraw-Hill, New York, 2019).
[22]A. T. Powis and I. D. Kaganovich, Phys. Plasmas **31**, 023901 (2024).
[23]M. M. Hopkins, E. S. Piekos, L. J. DeChant, and P. T. D., "Hybrid plasma modeling," Technical Report SAND2009-0963 (Sandia National Laboratories, 2009).
[24]Z. Donko, A. Derzsi, M. Vass, B. Horvath, S. Wilczek, B. Hartmann, and P. Hartmann, Plasma Sources Sci. Technol. **30**, 095017 (2021).
[25]M. H. L. van der Velden, W. J. M. Brok, J. J. A. M. van der Mullen, W. J. Goedheer, and V. Banine, Phys. Rev. E **73**, 036406 (2006).
[26]D. I. Astakhov, W. J. Goedheer, C. J. Lee, V. V. Ivanov, V. M. Krivtsun, A. I. Zotovich, S. M. Zyryanov, D. V. Lopaev, and F. Bijkerk, Plasma Sources Sci. Technol. **24**, 055018 (2015).
[27]M. A. van de Kerkhof, A. M. Yakunin, D. Astakhov, M. van Kampen, R. van der Horst, and V. Banine, J. Micro/Nanopattern. Mater. Metrol. **20**, 033801 (2021).
[28]T. Piskin, V. Volynets, H. Lee, S. K. Nam, and M. J. Kushner, Plasma Sources Sci. Technol. **34**, 125007 (2025).
[29]S. Sayan, K. Chakravorty, Y. Teramoto, B. Santos, A. Nagano, N. Ashizawa, T. Shirai, S. Morimoto, H. Watanabe, K. Aoki, and Y. Sato, Proc. SPIE **PC12494**, PC124940E (2023).
[30]Y. Teramotoi, S. Sayan, K. Chakravorty, T. Shirai, S. Morimoto, H. Watanabe, and Y. Sato, *Source Workshop*, *Source Workshop Proceedings* (EUV Litho, Inc., 2020). https://www.euvlitho.com/2020/2020%20Source%20Workshop%20Proceedings%20-%20Text%20Only.pdf
[31]K. Umstadter, M. Graham, M. Purvis, A. Schafgans, J. Stewart, P. Mayer, and D. Brown, Proc. SPIE **12494**, 124940Z (2023).
[32]R. M. van der Horst, J. Beckers, E. A. Osorio, D. I. Astakhov, W. J. Goedheer, C. J. Lee, V. V. Ivanov, V. M. Krivtsum, K. N. Koshelev, D. V. Lopaev, F. Bijkerk, and V. Y. Banine, J. Phys. D: Appl. Phys. **49**, 145203 (2016).
[33]J. Beckers, T. van de Ven, R. van der Horst, D. Astakhov, and V. Banine, Appl. Sci. **9**, 2827 (2019).
[34]J. van Veldhoven, A. Stodolna, P. van der Walle, Z. Bouza, J. Byers, O. Versolato, and M. Bayraktar, *Source Workshop, Source Workshop Proceedings* (EUV Litho, Inc., 2023). https://www.euvlitho.com/2023/2023%20Source%20Workshop%20Proceedings.pdf
[35]A. B. Langdon, J. Comput. Phys. **12**, 247 (1973).
[36]D. I. Astakhov, W. J. Goedheer, C. J. Lee, V. V. Ivanov, V. M. Krivtsun, K. N. Koshelev, D. V. Lopaev, R. M. van der Horst, J. Beckers, E. A. Osorio, and F. Bijkerk, J. Phys. D: Appl. Phys. **49**, 295204 (2016).
[37]D. Astakhov, "Numerical study of extreme-ultra-violet generated plasmas in hydrogen," Ph.D. thesis (University of Twente, Netherlands, 2016).
[38]K. N. Kenichi Nanbu, Jpn. J. Appl. Phys. **33**, 4752 (1994).
[39]M. S. Mokrov and Y. P. Raizer, Tech. Phys. **53**, 436 (2008).
[40]M. J. Brunger and S. J. Buckman, Phys. Rep. **357**, 215 (2002).
[41]T. W. Shyn, W. E. Sharp, and Y.-K. Kim, Phys. Rev. A **24**, 79 (1981).
[42]B. L. Peko and R. L. Champion, J. Chem. Phys. **107**, 1156 (1997).
[43]T. Simko, V. Martisovits, J. Bretagne, and G. Gousset, Phys. Rev. E **56**, 5908 (1997).
[44]Y. M. Chung, E. M. Lee, T. Masuoka, and J. A. R. Samson, J. Chem. Phys. **99**, 885 (1993).
[45]J. W. Gallagher, C. E. Brion, J. A. R. Samson, and P. W. Langhoff, J. Phys. Chem. Ref. Data **17**, 9 (1988).
[46]R. H. Day, P. Lee, E. B. Saloman, and D. J. Nagel, J. Appl. Phys. **52**, 6965 (1981).
[47]B. L. Henke, J. A. Smith, and D. T. Attwood, J. Appl. Phys. **48**, 1852 (1977).
[48]M. van de Kerkhof, A. M. Yakunin, V. Kvon, S. Cats, L. Heijmans, M. Chaudhuri, and D. Asthakov, J. Micro/Nanopattern. Mater. Metrol. **20**(1), 013801 (2021).
[49]T. H. M. van de Ven, P. Reefman, C. A. de Meijere, R. M. van der Horst, M. van Kampen, V. Y. Banine, and J. Beckers, J. Appl. Phys. **123**, 063301 (2018).
[50]J. Beckers, T. H. M. van de Ven, C. A. de Meijere, R. M. van der Horst, M. van Kampen, and V. Y. Banine, Appl. Phys. Lett. **114**, 133502 (2019).
[51]M. Osiac, T. Schwarz-Selinger, D. O'Connell, B. Heil, Z. L. Petrovic, M. M. Turner, T. Gans, and U. Czarnetzki, Plasma Sources Sci. Technol. **16**, 355 (2007).
[52]E. Kemaneci, J.-P. Booth, P. Chabert, J. van Dijk, T. Mussenbrock, and R. P. Brinkmann, Plasma Sources Sci. Technol. **25**, 025025 (2016).

22 April 2026 10:55:52

© Author(s) 2026